2

Surface Micro Topography Measurement Using Interferometry

Dahi Ghareab Abdelsalam
Engineering and Surface Metrology Laboratory,
National Institute for Standards,
Egypt

1. Introduction

Surface topography measurement plays an important role in many applications in engineering and science. The three dimensional (3D) shapes of objects need to be measured accurately to ensure manufacturing quality. Optical methods have been used as metrological tools for a long time. They are non-contacting, non-destructive and highly accurate. In combination with computers and other electronic devices, they have become faster, more reliable, more convenient and more robust. Among these optical methods, interferometry has received much interest for its shape measurement of optical and non-optical surfaces. Information about the surface under test can be obtained from interference fringes which characterize the surface. Two-beam interference fringes have been used to investigate the shape of optical and non-optical surfaces for a long time (Born et al., 1980). Phase distribution is encoded in an intensity distribution as a result of interference phenomena, and is displayed in the form of an interference pattern. Phase distribution should therefore be retrievable from the interference pattern. There are many methods of phase evaluation. In this chapter, we present recent developments in interferometry techniques carried out in our laboratory. In Sec. 2, the flat fielding method for coherent noise suppression is described. In Sec. 3, a combination of flat fielding and apodized apertures is presented. In Sec. 4, the phase retrieval using single-shot off-axis geometry, Zernike's polynomial fitting, Bünnagel's method, phase shifting interferometry, and two-wavelength interferometry are described. Section 5 describes a new off-axis interferometry configuration and the principle of single-shot, dual-wavelength interferometry for measuring a step height of 1.34 μm nominally. In Sec. 6, a multiple-beam interferometry technique at reflection for measuring the microtopography of an optical flat nominally of $\lambda / 20$ is described. Section 7 gives concluding discussions and remarks.

2. Flat fielding

The use of digital detectors in digital holography for recording a series of iterferograms is usually accompanied by dark current (thermal noise), shot noise, and scattering noise due to some dust particles, scratches, etc., on optical elements. Such coherent noise can affect the

quality of the reconstruction of the object wave (amplitude and phase). Subtracting the dark current (thermal noise) clears the camera of any accumulated charge and reads out the cleared CCD. Figure.1(a) shows a three-dimensional (3D) thermal noise captured when there is no illumination through the optical system. Figure.1(b) shows a 3D influence of the non-uniformity of illumination which is mainly caused by the non-uniform Gaussian intensity distribution, instability of the laser source used, and the vignetting of lenses used in the system. Some factors which cause coherent noise have been reduced drastically by application of the flat fielding method.

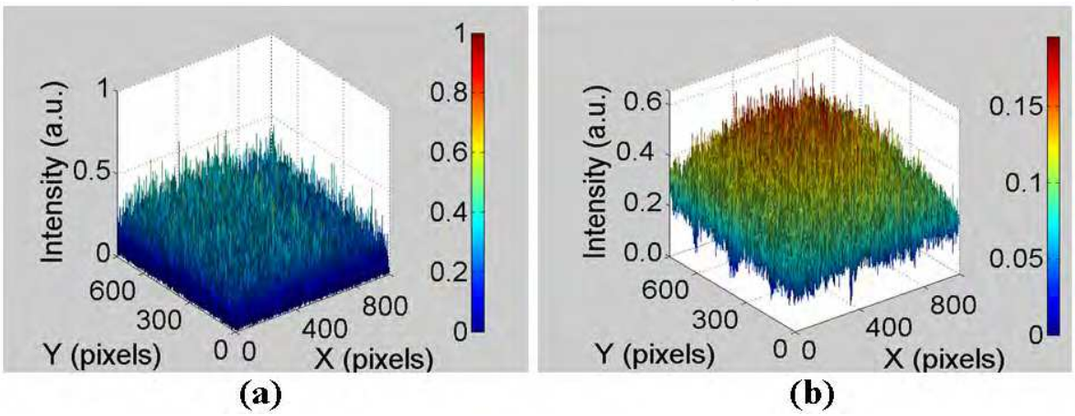

Fig. 1. Three-dimensional (3D) intensity distribution shows the effect of (a) dark frame (thermal noise), (b) influence of the non-uniformity of illumination (flat frame).

A CCD camera is calibrated by a process known as "Flat fielding" or "Shading correction". Flat fielding can be illustrated in the following formula (Abdelsalam et al., 2010; Steve, 2006; Abdelsalam et al., 2010),

$$\bar{I}_C = [M(\bar{I}_R - \bar{I}_B)] / (\bar{I}_F - \bar{I}_B), \tag{1}$$

where $\bar{I}_C$ is the average of calibrated captured interferograms, $\bar{I}_R$ is the average of non-calibrated captured interferograms, $\bar{I}_B$ is the average of dark frames, M is the average pixel value of the corrected flat field frame, and $\bar{I}_F$ is the average of flat field frames. Dark frames have been taken in advance and stored in the computer when there is no illumination through the optical system. Subtracting the dark frame clears the camera of any accumulated charge and reads out the cleared CCD. Flat field frames measure the response of each pixel in the CCD array to illumination and is used to correct any variation in illumination over the CCD sensor. The non-uniformity of illumination is mainly caused by the non-uniform Gaussian intensity distribution, as depicted in Fig.2(a). And also, the vignetting of lenses used in the system, which decrease the light intensity towards the image periphery or the dust particles on optical components like a glass window in front of CCD as illustrated in Fig.2(b), can be some inherent sources of errors in practical experiments. The flat fielding process corrects the uneven illumination.

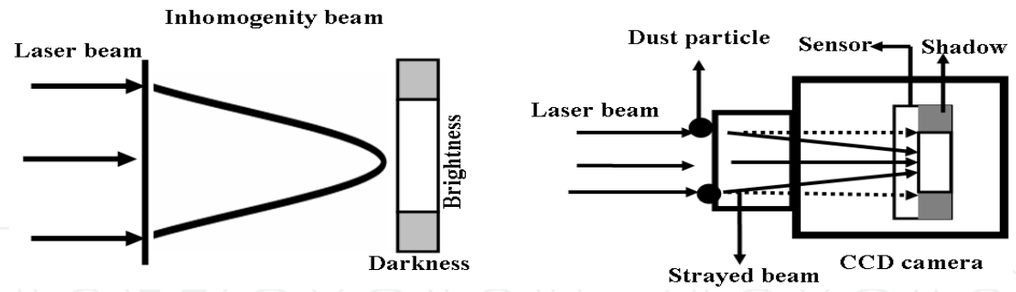

(a) (b)

Fig. 2. Uneven illumination which produces darkness at the edges of the image (a) inhomogenity of the laser beam, (b) shadow detection of the dust particles hanging at the CCD camera aperture.

Flat field frames are also captured in advance and stored in the computer by blocking the wave from the object arm. Note that flat field frames are captured when laser source is switched on. The captured single off-axis interferograms have been calibrated by using the stored dark and flat field frames. The specimen is a sample of 200 μm step height. Figure 3(a) shows an average of 50 off-axis interferograms $\bar{I}_R$ captured when the sample is adjusted as an object in the Mach-Zender interferometer. In order to subtract the thermal noise, fifty dark frames $\bar{I}_B$ have been captured when there is no illumination through the optical system. Shot noise (random arrival of photons), fixed pattern noise (pixel to pixel sensitivity variation), and scattering noise due to some dust particles or scratches on optical elements have been suppressed drastically when the flat fielding Eq.5 is applied. Where $\bar{I}_F$ is the average of 50 off-axis interferograms captured by blocking the wave from the object arm when laser source is switched on. Figure 3(b) shows the correction of Fig.3(a) after application of the flat fielding method.

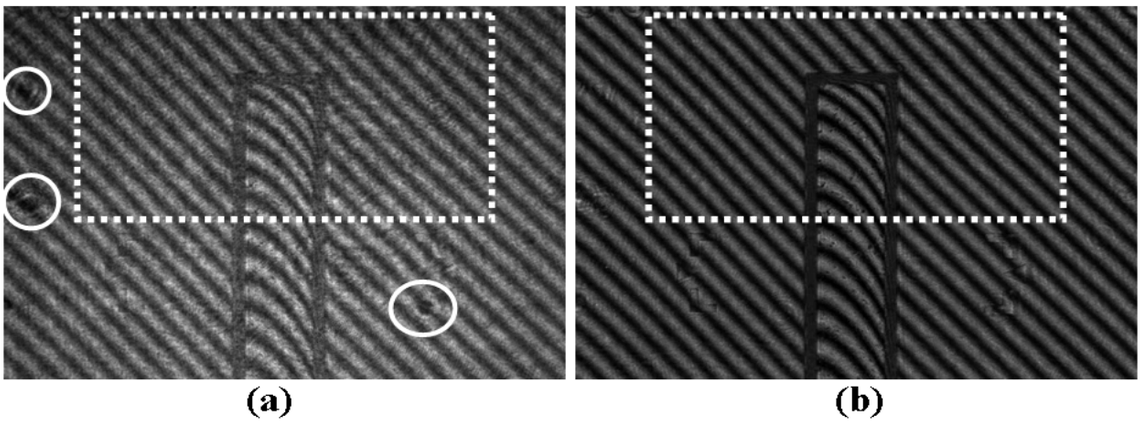

(a) **(b)**

Fig. 3. Average of 50 off-axis interferograms of a specimen of 200 μm step height. (a) Before correction with flat fielding. (b) After correction with flat fielding.

It is shown apparently from Fig.3(b) that most of random coherent noise (i.e. circulated noise which may come from dust particles and scratches) which distorts the holographic fringe pattern is reduced drastically by application of the flat fielding method.

3. Flat fielding with apodized aperture

The coherent noise is further reduced when the apodization with cubic spline interpolation technique (Cuche et al., 2000) is applied to the calibrated interferogram with flat fielding (Abdelsalam et al., 2011). Apodization of the interferogram could be achieved experimentally by inserting an apodized aperture in front of the CCD. However, as a digital image of the interferogram is acquired, it is more practical to perform this operation digitally by multiplying the digitized interferogram with a 2D function representing the transmission of the apodized aperture (this is explained in more detail in ((Cuche et al., 2000)). A profile of this function is presented in Fig.4(a). The aperture is completely transparent (transmission equal to unity) in the large central part of the profile. At the edges, the transmission varies from zero to unity following a curve defined by a cubic spline interpolation. After application of the apodized aperture technique to the corrected interferogram with flat fielding (Fig.3(b)), the obtained off-axis interferogram is numerically processed (Gabor, 1948; Kühn et al., 2007) to obtain the object wave (amplitude and phase). Figure 4(b) shows the reconstructed amplitude-contrast image after application of the flat fielding method with the apodized aperture technique.

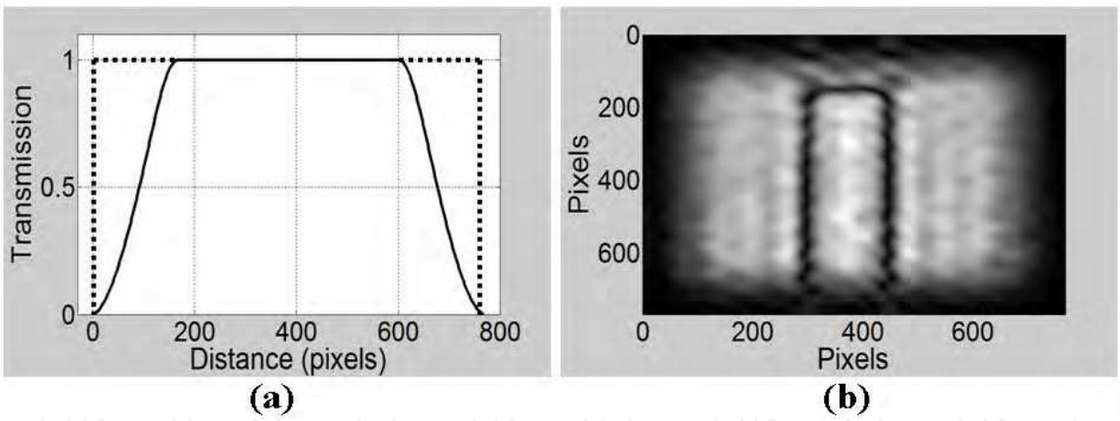

Fig. 4. Transmission profile of the apodized aperture. (a) The transmission from 0 to 1 at the edge of the aperture follows a cubic spline interpolation; the dashed line indicates the transmission of the unapodized aperture. (b) Numerically reconstructed amplitude-contrast image of Fig.3(b).

Figure 5(a) and Fig.5(b) show the reconstructed phase of the original off-axis interferogram (before correction) and after application of the proposed method (a combination of the flat fielding method with the apodized aperture technique), respectively. It can be noticed that the quality of the reconstructed phase-contrast image is improved as shown clearly in Fig.5(b) and Fig.5(d). The reconstructed phase images shown in Fig.5(a) and Fig.5(b) are exactly in the same size inside the white rectangles in Fig.3(a) and Fig.3(b), respectively.

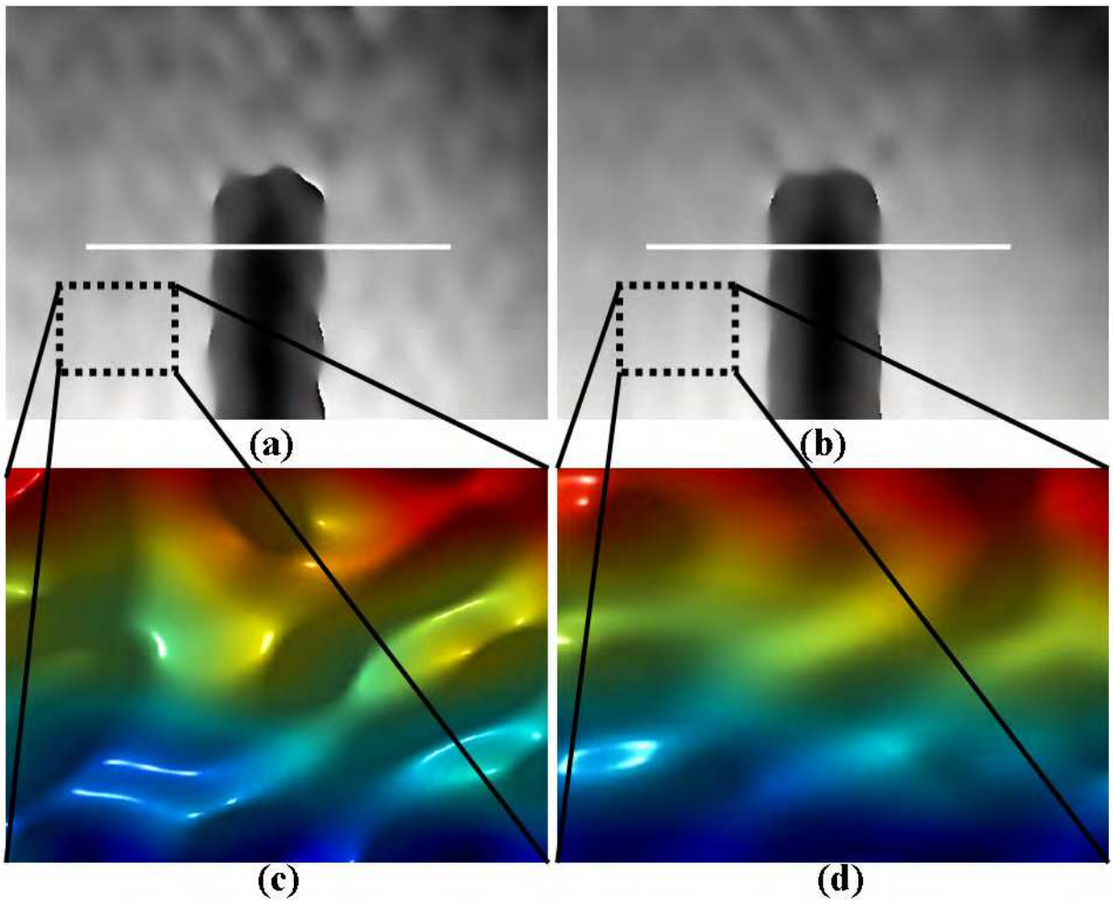

Fig. 5. Reconstructed phase images after converting to height from the off-axis interferograms. (a) Original (before correction with the proposed method). (b) After correction with the proposed method. (c) 3D of the selected rectangle of (a). (d) 3D of the selected rectangle of (b).

4. Phase retrieval

4.1 Off-axis geometry

In this section, the phase of single-shot circular fringes is extracted by using the off-axis geometry. Figure 6 shows the schematic diagram of the optical setup of the Fizeau interferometer (Abdelsalam et al., 2010). The tested smooth spherical surface of 25.4 mm in size was mounted as an object in the interferometer. A laser diode beam passes through a collimating lens and expands. This expansion is necessary to illuminate a greater area of the surface to be imaged and to reduce the error measurement due to the inhomogeneity in the Gaussian beam. The collimated beam of the laser light ($\lambda = 635nm$) falls upon the beam splitter, which transmits one half and reflects the other half of the incident light. The reflected collimated beam is then incident on the interferometer, which changes the path length of the light inside it due to the irregularities of the surface of the interferometer. When the object and the reference ($\lambda/20$ flatness) are mounted close and parallel, two types of circular reflection fringes are seen; one, called the insensitive fringes, due to the

interference from the two interfaces of the object surfaces, and the second, called the sensitive fringes, due to the interference of the reference interfaces and the object interfaces,. When 2D-FFT was applied for the inteferogram that had the two types of fringes (insensitive and sensitive) as shown in Fig. 7(a), six spectra were produced as shown in Fig. 7(b): three spectra produced from the insensitive fringes and the others produced from the sensitive fringes. In this case, the complex fringe amplitude becomes difficult to determine because the Fourier spectra of the interferogram that contains the insensitive and the sensitive fringes are not separated completely. The problem of the insensitive fringes was solved by adjusting the object so that it became parallel to the reference (in-line scheme). Therefore, the insensitive circular reflection fringes were seen in the center of the field of view. These circular fringes were transformed to a background spectrum (DC term) when 2D-FFT was applied (Cuche et al., 1999). By tilting the reference (off-axis case) as shown in Fig. 6, the sensitive circular reflection fringes were displaced, and nearly curved fringes at reflection with higher spatial frequency were seen, as shown in Fig.7(c). Only three spectra were obtained as shown in Fig.7(d) from Fig. 7(c) when 2D-FFT was implemented.

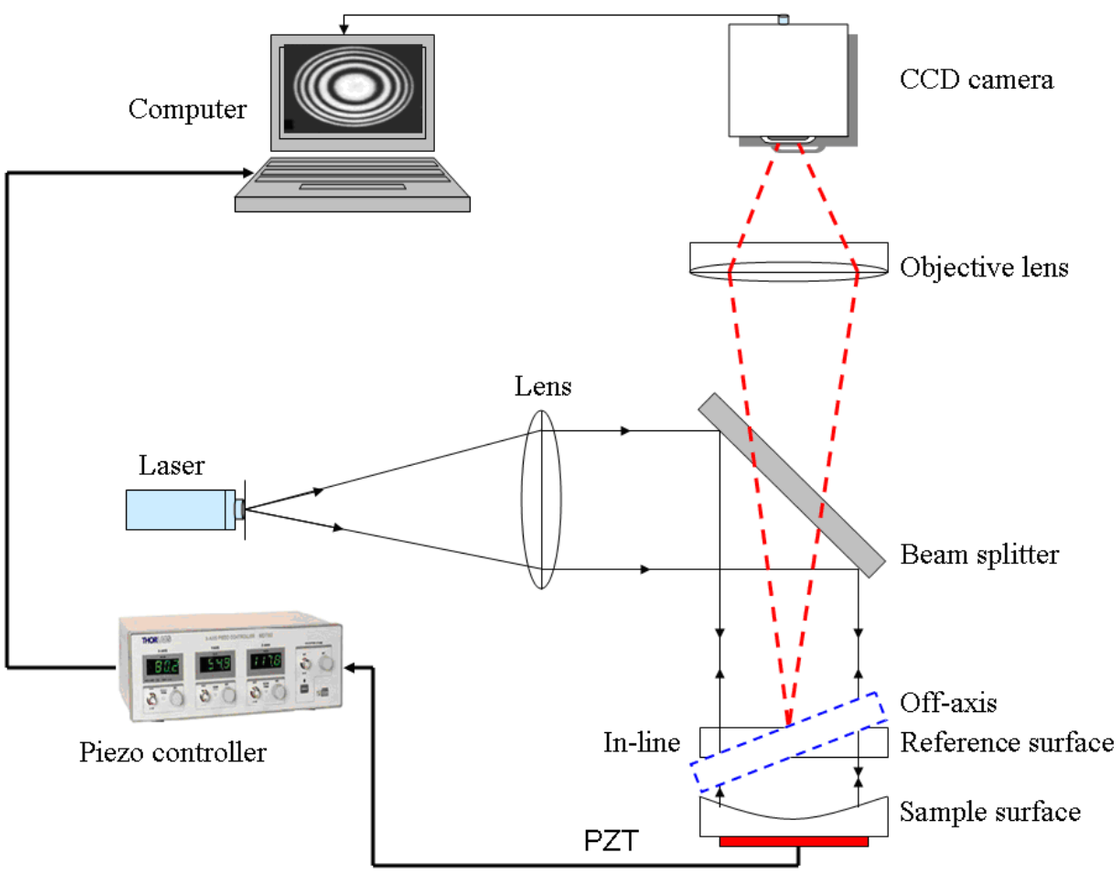

Fig. 6. Schematic diagram of the optical setup.

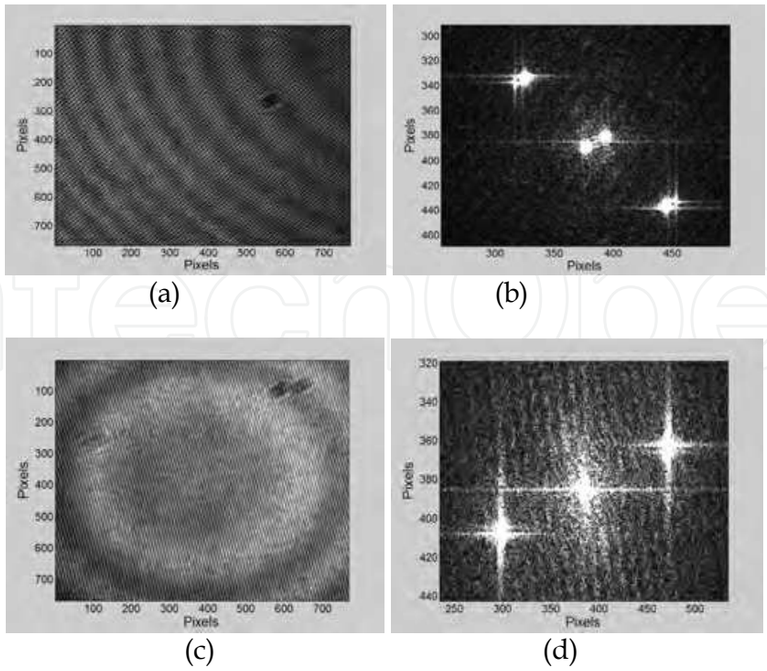

Fig. 7. Captured interferograms and their spectra using 2D-FFT. (a) Off-axis insensitive and sensitive fringes. (b) Spectra of (a). (c) In-line insensitive fringes and off-axis sensitive fringes. (d) Spectra of (c).

The interferogram was captured by the CCD camera of 1024×768 pixels with pixel size $\Delta x = \Delta y = 6.4\mu m$. Assume that the coordinate system of the interferogram plane is the *mn* plane. When waves from both the object and reference of the interferometer meet to interfere, the intensity of the interferogram is given as follows:

$$I(m,n) = \Psi = R^{*}O \cdot \tag{2}$$

Here, Ψ represents the intensity of the recorded interferogram, O is the object beam, R is the reference beam,* denotes the complex conjugate and *m, n* are integers. The reconstructed wave front is an array of complex numbers. An amplitude-contrast image and a phase-contrast image can be obtained by using the following intensity $[\mathrm{Re}(\Psi)^2 + \mathrm{Im}(\Psi)^2]$ and the argument $\tan^{-1}[\mathrm{Re}(\Psi) / \mathrm{Im}(\Psi)]$, respectively. In the reconstruction process, the intensity of the interferogram is multiplied by the amplitude of the original reference wave called a *digital reference wave* ($R_D(m,n)$). If we assume that a perfect plane wave is used as the reference for interferogram recording, the computed replica of the reference wave $R_D(m,n)$ can be calculated as follows:

$$R_D(m,n) = A_R \exp[i(2\pi / \lambda)(k_x m\Delta x + k_y n\Delta y)] . \tag{3}$$

Where, A_R is the amplitude, λ is the wavelength of the laser source, and k_x and k_y are the two components of the wave vector that must be adjusted such that the propagation direction of $R_D(m,n)$ matches as closely as possible with that of the experimental reference wave. By using this digital reference wave concept, we can obtain an object wave which is

reconstructed in the central region of the observation plane. The captured interferogram of the surface object was processed using Matlab codes to obtain a reconstructed object wave (amplitude and phase). Figure 8 shows the detail numerical reconstruction process of a single shot off-axis hologram of a surface object. As depicted in Fig. 8(a) through 8(d), 2D-FFTs were implemented for the spatial filtering approach. The inverse 2D-FFT was applied after filtering out the undesired two terms, and the complex object wave depicted in Fig. 8(d) and 8(e) in the interferogram plane was extracted. After the spatial filtering step, the object wave in the interferogram plane was multiplied by the digital reference wave $R_D(m,n)$. The final reconstructed object wave (amplitude and phase) as demonstrated in Fig. 8(g) and 8(h) was recorded by selecting appropriate values for the two components of the wave vector $k_x = 0.002955mm^{-1}$ and $k_y = 0.01143mm^{-1}$. The reconstructed phase shown in Fig. 8(h) is non-ambiguous and shows the results wrapped onto the range $-\pi$ to π. In order to retrieve the continuous form of the phase map ϕ, an unwrapping step has to be added to the phase retrieval process (Ghiglia et al., 2010).

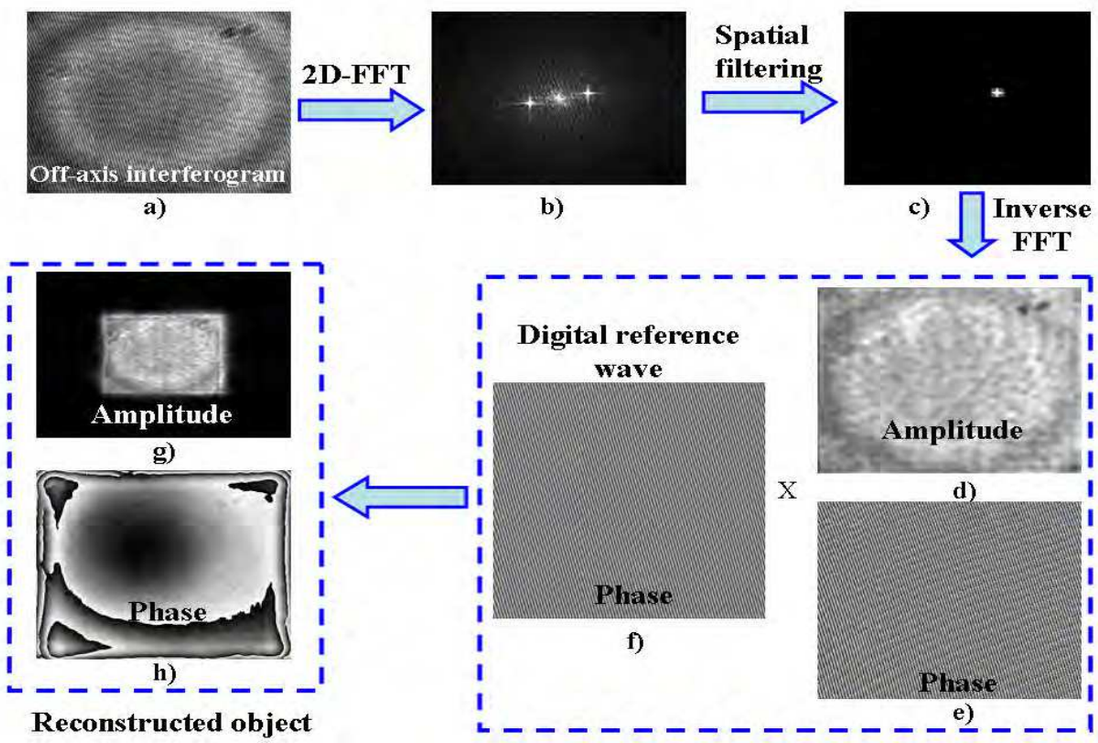

Fig. 8. Reconstruction steps of the conventional spatial filtering based phase contrast off-axis interferometry: a) Off-axis interferogram, b) Fourier transformed spatial frequency domain data, c) Spatially filtered domain data, d) – e) Inversely Fourier transformed data, f) Phase map of the digital reference wave, g) – h) Reconstructed object wave.

The two-dimensional (2D) surface profile height *h* can be calculated directly as follows:

$$h = \frac{\phi}{4\pi}\lambda . \tag{4}$$

Figure 9(a) shows the 480×480 pixels unwrapped phase map for the wrapped phase map in Fig. 8(h). The 3D view of the unwrapped phase map is shown in Fig. 9(b).

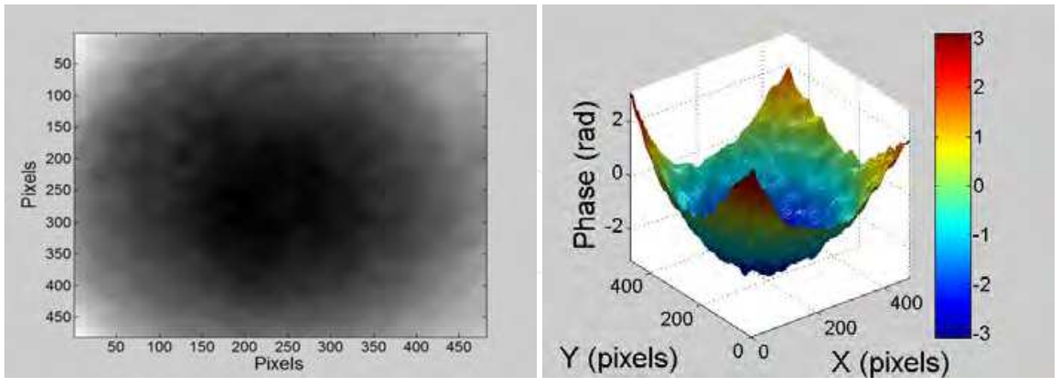

(a) (b)

Fig. 9. (a) 480 x 480 pixels unwrapped phase map for the wrapped phase map in Fig.4(h). (b) Three-dimensional view of the unwrapped phase map of (a).

The phase information shown in Fig. 9(b) was converted to metrical 3D surface height information as shown in Fig.10(a). Figure 10(b) presents the measured profile curve along 450 pixels in the x-direction and its cubic fitting.

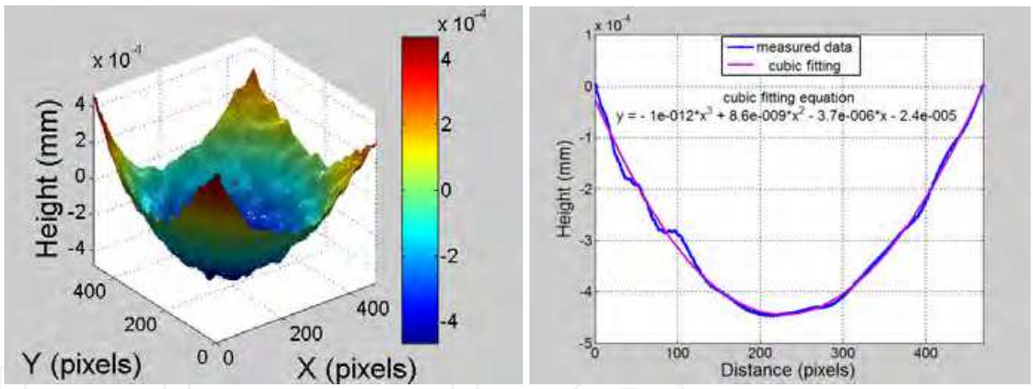

(a) (b)

Fig. 10. (a) Three-dimensional surface height resulting from the unwrapped phase shown in Fig. 9(b). (b) Two-dimensional surface height along 450 pixels in the x-direction.

The peak to valley value calculated from Fig. 10(b) was of the order of $0.45x10^{-3}mm$.

4.2 Zernike's polynomial fitting

Zernike polynomials have been used extensively to fit wavefront data for the interferometry to obtain an accurate representation of the surface. The characteristics of the surface are described by the calculation of the weighting coefficients of the Zernike polynomials. The surface height function $Z_r(x_r, y_r)$ can be represented by a linear combination of M polynomials $F(x_r, y_r)$ and their weighting coefficients G (David, et al., 1993 ; Wang, et al., 1980) is expressed as follows:

$$Z_r(x_r, y_r) = \sum_{j=1}^{M} F_j(x, y) G_j \ , \tag{5}$$

where r is the sample index so, it is important to calculate the coefficients to represent the surface. This can be done by thinning and ordering the fringes, respectively. A computer program with Matlab was written to obtain the thinning of the fringes. The fringe pattern is digitized into the computer and then thresholded to yield a binary gray-level image. The median filter was used to delete salt and pepper noise in the image. The flat fielding method was applied to the image to remove the effect of the offset of the camera and the inhomogeneity of the collimated laser beam intensity. The x-y scan suitable for the circular fringes was applied to the corrected image to obtain the fringe centers. After the fringes were thinned, the assignment of the fringe orders was determined. The flowchart of the algorithm is shown in Fig.11.

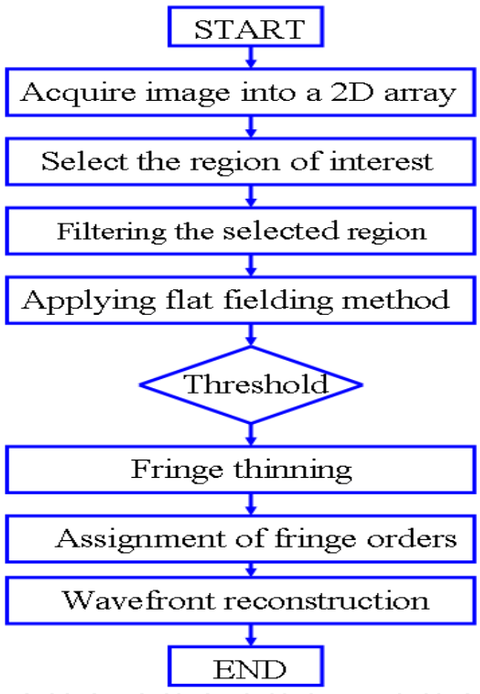

Fig. 11. Flow chart for the fringe pattern processing.

The data were fitted to a polynomial set. This is typically accomplished with a least-squares method, where S is defined as the sum of the square of the difference between the data points and the fitted polynomials is expressed as follows:

$$S = \sum_{r=1}^{N} \left[Z_r - \sum_{j=1}^{M} G_j F_j(x_r, y_r) \right]^2 . \tag{6}$$

If a perfect fit were possible, S would be equal to zero, because there would be no difference between the measured values and the representing polynomials evaluated at the corresponding points. However, there are always differences between the real surface and

its representation. Therefore S is nonzero. The function of a least-squares fit is to find the coefficients for a given set of polynomials, which minimizes S. The coefficients are found by taking the derivative of S with respect to each coefficient and setting the result equal to zero. The result of minimizing S for all coefficients can be expressed by using summations in matrix form as follows:

$$\begin{bmatrix} \sum_{r=1}^{N} Z_r F_1(x_r, y_r) \\ \vdots \\ \sum_{r=1}^{N} Z_r F_M(x_r, y_r) \end{bmatrix} = \begin{bmatrix} \sum_{r=1}^{N} F_1(x_r, y_r) F_1(x_r, y_r) \ldots\ldots \sum_{r=1}^{N} F_M(x_r, y_r) F_1(x_r, y_r) \\ \vdots \\ \sum_{r=1}^{N} F_1(x_r, y_r) F_M(x_r, y_r) \ldots\ldots \sum_{r=1}^{N} F_M(x_r, y_r) F_M(x_r, y_r) \end{bmatrix} \begin{bmatrix} G_1 \\ \vdots \\ G_M \end{bmatrix}. \quad (7)$$

The equations were solved numerically and G_j were obtained. The reconstruction of the surface was obtained automatically after substituting the coefficients in Eq.5. The same sample used in off-axis geometry has been adjusted in the in-line case of the setup shown in Fig.6. The captured interferogram is shown in Fig.12(a). The corrected fringe pattern with flat fielding shown in Fig.12(b) was processed by the automatic processing technique (see the flow chart in Fig.11) and the 3D surface profile of the surface under test was obtained automatically.

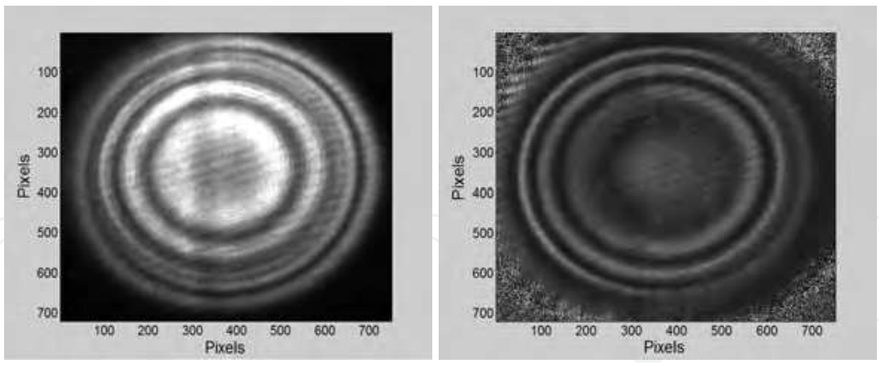

(a) (b)

Fig. 12. (a) Circular fringe pattern before correction with flat fielding. (b) After correction.

The 3D reconstruction surface of the circular fringe pattern of Fig.12(b) is shown in Fig.13(a). The 2D surface profile along 450 pixels in the x-direction and its cubic fitting is shown in Fig.13(b). The surface form of the tested spherical surface was estimated from Fig.13(b) to be of the order of $0.44x10^{-3}$ mm.

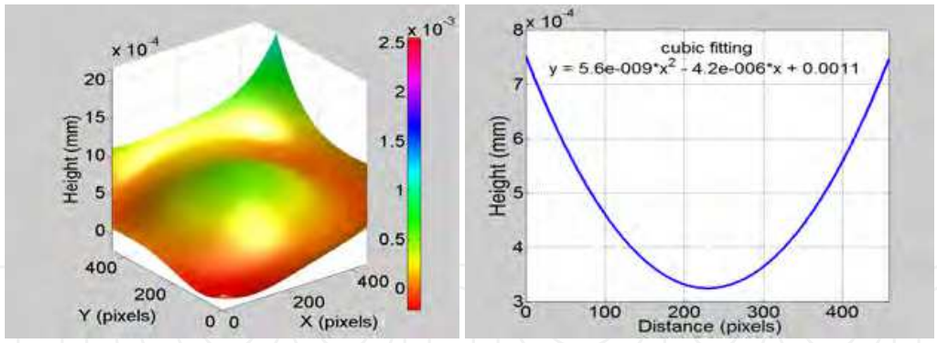

(a) (b)

Fig. 13. Processing results of the circle interference fringe pattern. (a) Three-dimensional reconstruction surface by using Zernike polynomial fitting method. (b) Two-dimensional surface profile.

4.3 Bünnagel's method

The Bünnagel method (Bünnagel, 1956) was used in this paper to analyze the interferogram of the tested smooth spherical surface. This method has been used to analyze multiple-beam interferograms with very sharp fringes manually. Nowadays, with the invention of high speed microprocessors and high speed CCD cameras, the Bünnagel method can be applied to two-beam interferograms. The feature height obtained from the Bünnagel method depends only on the fringe distance as shown in Eq.(11). From the schematic diagram shown in fig. 5, the topographical height related to fringe distance is calculated as follows:

$$h_2 = q\cos(\alpha),\ \tan(\alpha) = s / d_2,\ s + q = 2\lambda / 2, \tag{8}$$

when α is taken very small, so that $\cos(\alpha) = 1$. The height can be written as follows:

$$h_2 = 2\lambda / 2 - d_2 \tan(\alpha). \tag{9}$$

Also from fig.4, one can write $\tan(\alpha) = \dfrac{4\lambda / 2}{d_4}$ or

$$h_2 = \frac{\lambda}{2}\left(2 - \frac{d_2 / d_4}{4}\right), \tag{10}$$

or for general case

$$h_m = \frac{\lambda}{2}\left(m - \frac{d_m / d_n}{n}\right), \tag{11}$$

where h_m is the topographical height at fringe m.

d_m is the distance from fringe m to selected points AC and d_n is the distance from fringe n (at selected point B) to AC.

The same sample used in the off-axis geometry method has been adjusted in the in-line case of the setup shown in Fig.6. The captured interferogram is shown in Fig.12(a). The corrected fringe pattern with flat fielding is shown in Fig.12(b). Three fringes from the center of the circular fringes shown in Fig.12(b) have been dealt with. Since the topographical height is related to the fringe distance as expressed in Eq.10, a line profile as shown in Fig.15(a) has been taken over the 3 fringes from the center of Fig.12(b). The source used in the experiment is a laser diode of $\lambda = 635nm$. The surface height at the center of the 3 fringes has been calculated by using Eq.11. The 2D surface profile along 450 pixels in the x-direction and its cubic fitting is shown in Fig.15(b). The surface form of the tested spherical surface was estimated from Fig.13(b) to be of the order of $0.46x10^{-3}$ mm.

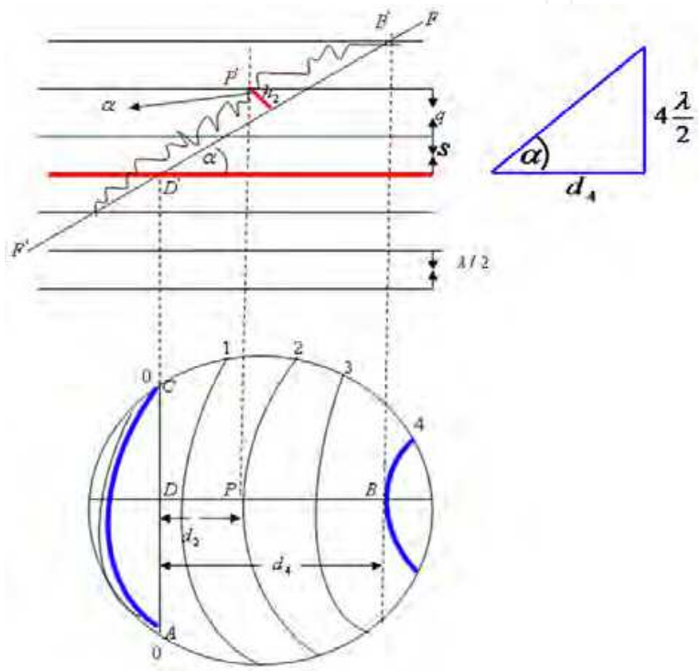

Fig. 14. Schematic diagram of the interferogram and height description.

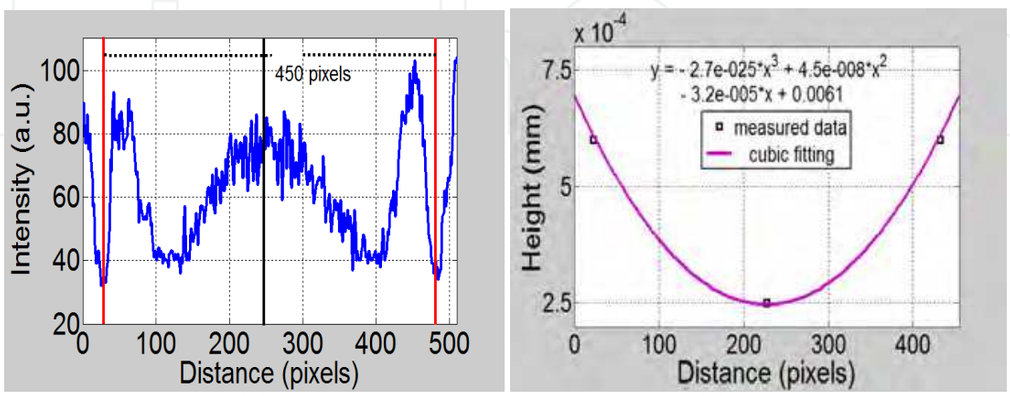

(a) (b)

Fig. 15. (a) Intensity profile taken in the middle of Fig.12(b). (b) Two-dimensional surface profile.

4.4 Phase shifting algorithms

Phase shifting is a very robust technique for the analysis of fringe patterns. Phase shifting measures the phase of a pixel depending on the values of that pixel in different images. The intensity distribution of the phase-shifted frames for the initial state of the object can be expressed as follows:

$$I(x,y) = I_O + I_R + 2\sqrt{I_O I_R}\cos(\varphi + j\pi / 2), \tag{12}$$

where I_O and I_R are the intensities of the object and the reference waves, respectively, φ is the phase, and j is the number of the phase-shifted frames. Several phase-shifting algorithms have been developed with a view to reduce the effect of the phase shift and other errors on phase calculation (Kumar, et al., 2009). The evaluated phase is wrapped between $-\pi$ and π due to arctangent function. In this section we present a comparative study of several of these algorithms in fringe analysis.

4.4.1 Three-step algorithm

Using the first stored phase-shifted frames ($j = 0-2$), the phase distribution of the object can be expressed as follows (Kumar, et al., 2009):

$$\phi_j = \tan^{-1}\left(\frac{I_1 - 2I_2 + I_3)}{I_1 - I_3}\right), \tag{13}$$

4.4.2 Four-step algorithm

It uses the first four stored phase-shifted frames ($j = 0-3$). The phase distribution can be expressed as follows (Kumar, et al., 2009):

$$\phi_j = \tan^{-1}\left(\frac{(I_2 - I_4)}{-I_1 + I_3}\right). \tag{14}$$

4.4.3 Five-step algorithm

From the first five stored phase-shifted frames ($j = 0-4$). The phase distribution can be written as follows (Kumar, et al., 2009):

$$\phi_j = \tan^{-1}\left(\frac{2(I_2 - I_4)}{-I_1 + 2I_3 - I_5}\right). \tag{15}$$

4.4.4 Six-step algorithm

If we use the first six stored phase-shifted frames ($j = 0-5$). The phase distribution can be expressed as follows (Kumar, et al., 2009):

$$\phi_j = \tan^{-1}\left(\frac{I_1 - I_2 - 6I_3 + 6I_4 + I_5 - I_6)}{4(I_2 - I_3 - I_4 + I_5)}\right) - \frac{\pi}{4}. \quad (16)$$

4.4.5 Seven-step algorithm

Using all the seven stored phase-shifted frames (j=0–6), we have phase distribution as follows (Kumar, et al., 2009):

$$\phi_j = \tan^{-1}\left(\frac{4I_2 - 8I_4 + 4I_6)}{-I_1 + 7I_3 - 7I_5 + I_7}\right). \quad (17)$$

The tested surface (same sample used in the off-axis geometry method) was mounted as an object in the interferometer and adjusted very closely to the reference. The distance of the cavity between the object and the reference was changed very slightly by using a PZT varied by voltage. The four-step algorithm explained in section 4.4.2 is used to extract the phase. Four different interferograms with $0, \pi/2, \pi$ and $3\pi/2$ radian phase shifts were captured and corrected with the flat fielding method as shown in Fig.16.

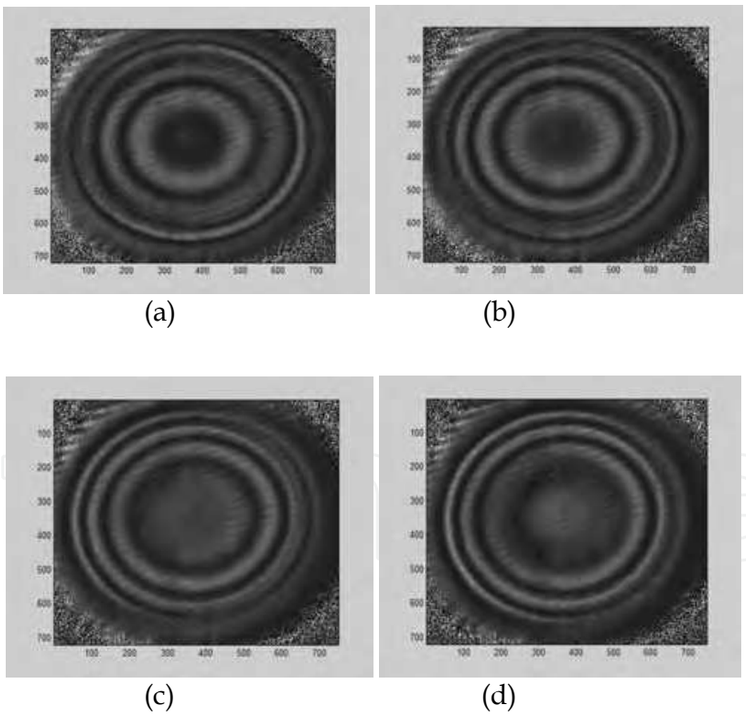

(a) (b)

(c) (d)

Fig. 16. Four different interferograms (x-axis and y-axis are pixels) with (a) 0, (b) $\pi/2$, (c) π, and (d) $3\pi/2$ radian phase shifts after correction with the flat fielding method.

The wrapped phase map (Eq.14 is used) from the corrected interferograms is shown in Fig.17(a). The wrapped phase map is then unwrapped to remove the 2π ambiguity and the unwrapped phase map is shown in Fig.17(b). Figure.17(c) shows 480 x 370 pixels

unwrapped phase map at the middle of Fig.17(b). The phase information shown in Fig.17(c) was converted to metrical 3D surface height information by using Eq.4 as shown in Fig.17(d).

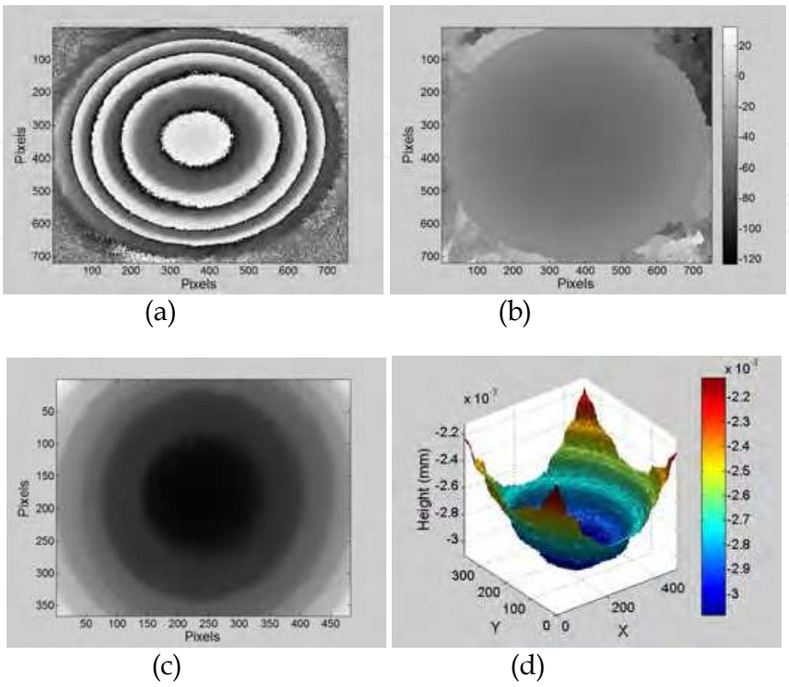

Fig. 17. (a) Wrapped phase map resulted from the four-frames. (b) Unwrapped phase information in 2D grey-scale. (c) 480 x 370 pixels unwrapped from the middle of (b). (d) Three-dimensional surface height of (c).

Figure.18 presents the measured profile curve along 450 pixels in the x-direction and its cubic fitting. The peak to valley value calculated from Fig.18 was of the order of $0.47x10^{-3}mm$.

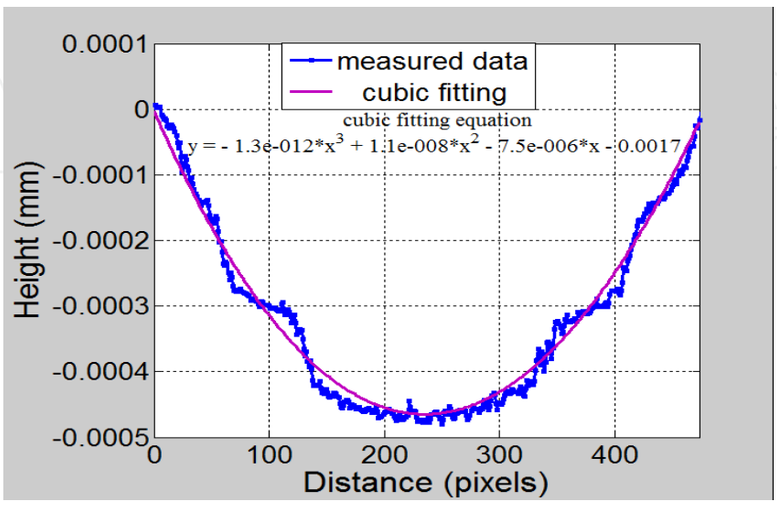

Fig. 18. Two-dimensional surface height along 480 pixels at x-direction.

As shown from the results and the cubic fitting equations, the measured value measured with off-axis geometry is very close to the value measured with the Zernike's polynomial fitting method, the Bünnagel's method, and the four-frame phase shifting technique. The little deviation may be due to the vibration because the phase shifting algorithm is more sensitive to vibration than single shot off-axis geometry.

4.5 Two-wavelength interferometry

The conventional interferometric surface profilers using a single wavelength (the phase takes the form of a sawtooth wave, as seen in Fig. 19) have a serious limitation: they can only handle smooth profiles and step heights of less than half a wavelength. The approaches adopted to overcome the problem of the small dynamic range are based on two-wavelength interferometry, multi-wavelength interferometry and white-light interferometry. In the two-wavelength method, the system can use long-range measurements with careful choice of wavelengths. If the phase of the surface under test is measured at two wavelengths, λ_1 and λ_2, then the difference between the two corresponds to the modulo-2π phase map, which could have been generated with a longer wavelength (synthetic beat-wavelength) expressed as follows:

$$\Lambda = \frac{\lambda_1 \lambda_2}{\lambda_2 - \lambda_1}. \tag{18}$$

We can see that the smaller the difference between the two wavelengths, the larger the synthetic wavelength, typically within the range of micrometers to millimeters. The resulting graph of a discontinuity in phase for two wavelengths before subtraction is shown in Fig.20. The algorithm for the unwrapping of phase discontinuities is simple; one wavelength is simply subtracted from the other, as seen in Fig. 21. The result appears to be discontinuous, but by merely adding 2π wherever the phase map is negative (addition modulo 2π), the result is a continuous slope that accurately recreates the original object.

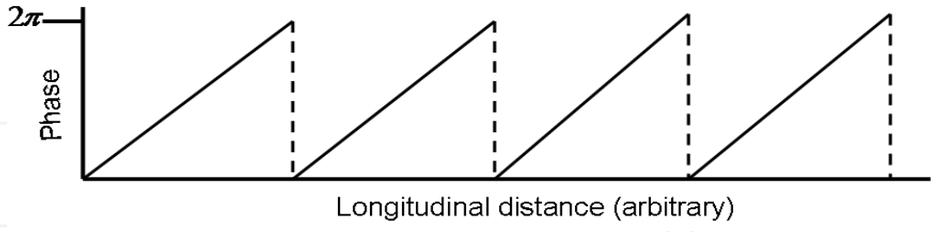

Fig. 19. Phase map of using one wavelength.

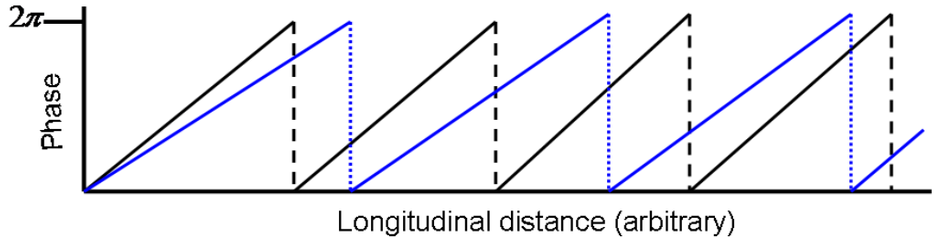

Fig. 20. Phase maps for two wavelengths.

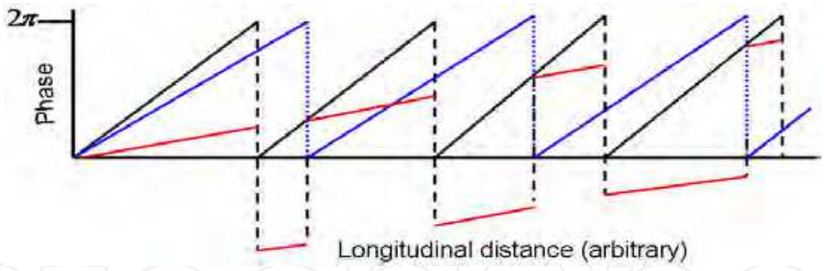

Fig. 21. Subtraction of phase maps.

5. Single-shot, dual-wavelength interferometry

5.1 Principle

The principle is based on the acquisition of an interferogram by a CCD camera with two object beams O_1 and O_2 of two different wavelengths λ_1 and λ_2 that interfere with two counterpart reference beams R_1 and R_2, emitted by the same pair of laser sources, in an off-axis configuration (Abdelsalam et al., 2011). The expression for the intensity pattern, which results from both interferomgrams at λ_1 and λ_2, can be written as follows:

$$I(k,l) = |O_1|^2 + |R_1|^2 + |O_2|^2 + |R_2|^2 + R_1^* O_1 + R_1 O_1^* + R_2^* O_2 + R_2 O_2^* . \quad (19)$$

Here, I is the interferogram intensity, k and l are integers, and * denote the complex conjugate. In Eq. (1), the first four intensity terms are of zero order, which can be directly filtered in the Fourier domain, and the last four are the interference terms with the object wave O_i (the virtual images) or their conjugate O_i^* (the real images), being modulated by the spatial carrier frequency in the spatial frequency domain. The carrier frequencies are dependent upon the k-vectors of R_1 and R_2. Now, if the two reference waves have different propagation directions, especially in the configuration where their k-vector projections on the CCD plane are orthogonal, each interference term occupies a different position in the Fourier domain. Provided that there is no overlap between the interference terms, it is straightforward to isolate each frequency component by the spatial filtering approach (Cuche et al., 2000). After filtering out the object and conjugate terms, $R_1^* O_1$ and $R_2^* O_2$, the filtered spectrum data in the spatial frequency domain turn back to the spatial domain by using inverse 2D FFT separately for each wavelength. Let us define these two filtered complex waves Ψ_1 and Ψ_2 as follows:

$$\Psi_i = R_i^* O_i , \quad (20)$$

where $i = 1,2$. The above filtered complex wave is an array of complex numbers. An amplitude-contrast image and a phase-contrast image can be obtained by using the following intensity $[\mathrm{Re}(\Psi_i)^2 + \mathrm{Im}(\Psi_i)^2]$ and the argument $\arctan[\mathrm{Re}(\Psi_i)/\mathrm{Im}(\Psi_i)]$, respectively. Finally, in order to obtain the object information, the Ψ_i needs to be multiplied by the original reference wave called a digital reference wave $(R_{D_i}(m,n))$. Here, m and n are integers. If we assume that a perfect plane wave is used as a reference for interferogram recording, the computed replica of the reference wave R_{D_i} can be represented as follows:

$$R_{D_i}(m,n) = A_{R_i} \exp[i(2\pi / \lambda_i)(k_{x_i} m\Delta x + k_{y_i} n\Delta y)], \tag{21}$$

where, A_{R_i} is the amplitude, λ_i is the wavelength of the laser source, $\Delta x = \Delta y$ are the pixel sizes, and k_{x_i} and k_{y_i} are the two components of the wave vector that must be adjusted such that the propagation direction of R_{D_i} matches as closely as possible with that of the experimental reference wave. By using this digital reference wave concept, we can obtain an object wave which is reconstructed in the central region of the observation plane for each wavelength separately. As stated above, the reconstructed complex wave fronts O_1 and O_2 in the reconstruction plane contain both the amplitude and the phase information. However, both complex wave fronts suffer from phase ambiguity for abrupt height varying specimens. In order to overcome this limitation of the single wavelength approach, we can use a synthetic beat-wavelength that can be defined as follows:

$$\Phi = \arg(O_1 O_2^*) = \phi_1 - \phi_2 = 2\pi x\left(\frac{\lambda_2 - \lambda_1}{\lambda_1 \lambda_2}\right) = 2\pi \frac{x}{\Lambda}, \tag{22}$$

where, x is OPD (Optical Path Difference), which means twice of the topography for reflection scheme. ϕ_i is the reconstructed phase for wavelength λ_i and Λ is the synthetic beat wavelength expressed in Eq.18. The two-dimensional (2D) surface profile height *h* can be calculated directly as follows:

$$h = \frac{\Phi}{4\pi}\Lambda. \tag{23}$$

Figure 22 shows the flow chart of the algorithm that has been used to analyze the off-axis interferogram containing both wavelengths.

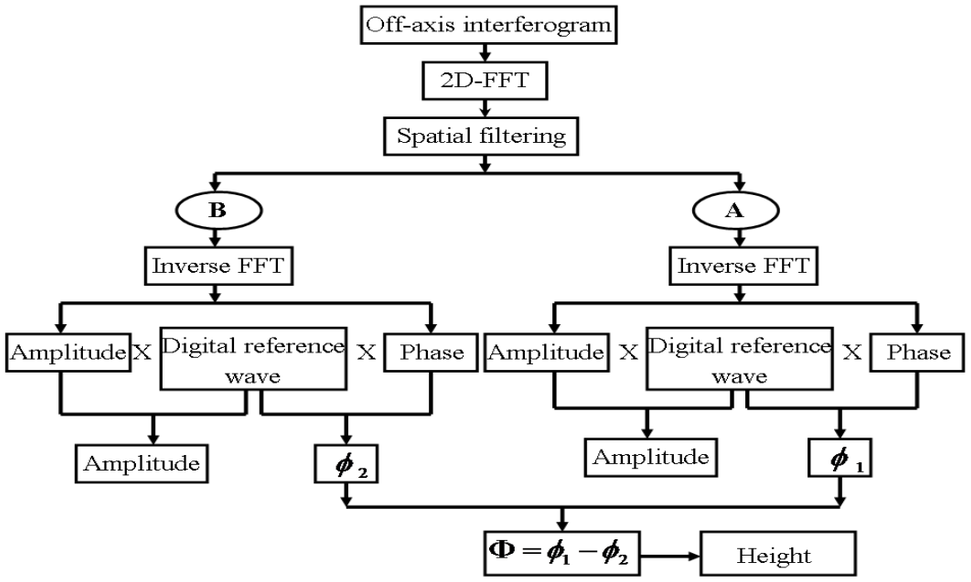

Fig. 22. Flowchart of the algorithm that has been used to analyze the off-axis interferogram containing both wavelengths.

5.2 Experimental results

The proposed new scheme on the dual-wavelength off-axis system which is basically based on a Mach-Zehnder interferometer is shown in Fig. 23. The laser sources used in the experiment are laser diodes with $\lambda_1 = 635nm$ and $\lambda_2 = 675nm$, yielding a synthetic wavelength $\Lambda = 10.72\mu m$. The key concept of the proposed scheme is to separate each wave wavelength beam pair in different reference arms, while combining them in an object arm. We employ two PBSs (Polarizing Beam Splitters) and two HWPs. Each laser beam is expanded by using a spatial filter and collimated by a collimating lens. An iris in front of the lens allows the adjustment of the size of the collimated beam. For the wavelength λ_1 , the laser beam is divided into object and reference beams through the PBS 1. After passing through the PBS 1, the transmitted beam becomes p-polarized (parallel to the optical plane) while the reflected beam gets s-polarized (perpendicular to the optical plane). The transmitted beam acts as the reference beam of the wavelength λ_1 and it travels to the CCD sensor maintaining the same linear p-polarization by the triangular prism and mirror 1. Meanwhile, the reflected one which is entitled to be the object beam meets a HWP which is designed for the wavelength λ_1 . By setting the optic axis of the HWP for rotation by 45 degrees from the s-polarization axis, we can rotate the linear polarization state by 90 degrees. The polarization state of the object wave for λ_1 is changed from s-polarization to p-polarization. After that, it passes through the PBS 2 and BS 2 to illuminate the surface of the object and travels to the CCD sensor. Likewise, for the wavelength λ_2 , the laser beam is divided into object and reference beams through PBS 2. After passing through the PBS 2, the transmitted beam becomes p-polarized (parallel to the optical plane) while the reflected beam gets s-polarized (perpendicular to the optical plane) exactly as done for λ_1 .

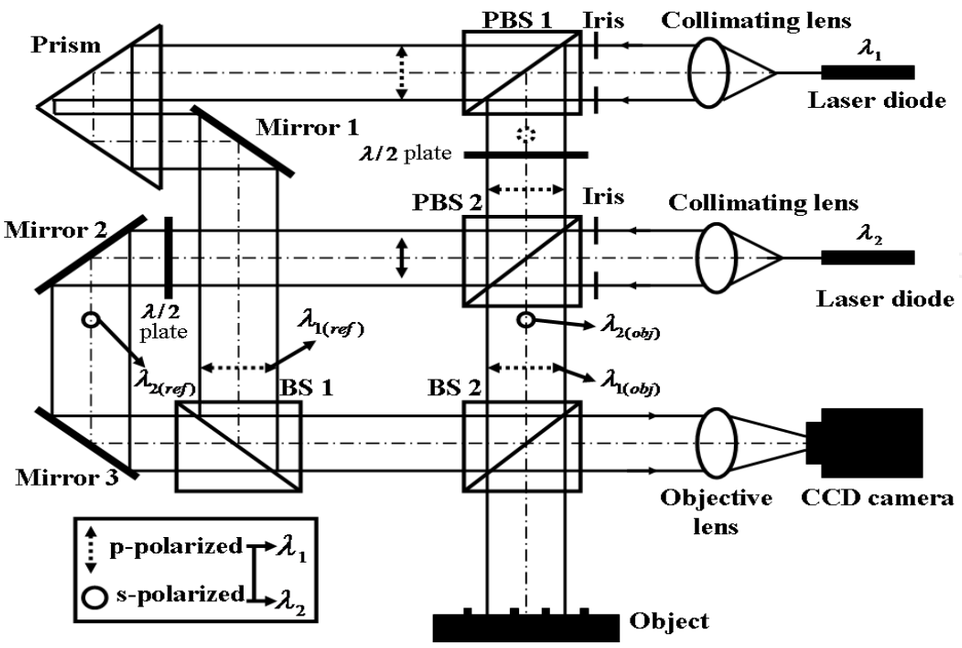

Fig. 23. Schematic diagram of the proposed single shot dual-wavelength interferometric system.

The transmitted beam corresponds to the reference beam of the wavelength λ_2 . But it meets a HWP which is designed for the wavelength λ_2 , and consequently, the polarization state is changed from p-polarization to s-polarization state when the optic axis of the HWP designed for the wavelength λ_2 is set for rotation by 45 degrees from the s-polarization axis, in the exactly same manner as in the case of λ_1 .Then, it travels to the CCD sensor maintaining the same linear s-polarization state. Meanwhile, the reflected beam, which is in the linear s-polarization state, remains unchanged and illuminates the surface of the object and then travels to the CCD sensor. Here, the object beam for both wavelengths illuminates the object, and the reflected object beam propagates on-axis with the light diffracted from the 3-D object. To obtain the off-axis interferogram, mirrors that reflect the reference waves R_1 and R_2 are tilted such that the reference wave reaches the CCD with an incidence angle while the object wave propagates perpendicular to the CCD. Finally, the CCD camera records the interferogram that result from the interference between the object wave O_1 and the reference wave R_1 . And also, the interference between the object wave O_2 and the reference wave R_2 is recorded simultaneously. Figure 24 shows the experimental results obtained through the proposed dual-wavelength off-axis interferometric scheme. The surface under test is an object with a nominal height 1.34 μm . The general procedure which is needed for measuring the complex object wave in dual-wavelength off-axis interferometry is shown in Fig.24. Both amplitude and phase information of the object for the two wavelengths can be obtained with a single interferogram. Figure 24 represents the experimental results of application of the 2D-FFT based spatial filtering method for each wavelength separately. After the spatial filtering step, the digital reference wave R_{D_i} is used for the centering process. Then, the final reconstructed object is obtained by adjusting the values of k_x and k_y for each wavelength separately.

The digital reference wave used in the calculation process should match as close as possible to the experimental reference wave. This has been done in this paper by selecting the appropriate values of the two components of the wave vector k_x = 0.00819 mm^{-1} and k_y = -0.00654 mm^{-1} for the interferogram captured at $\lambda_1 = 635nm$ and k_x = -0.09944 mm^{-1} and k_y = 0.00674 mm^{-1} for the interferogram captured at $\lambda_2 = 675nm$. Once the two phase maps are obtained for each wavelength, a phase map can be calculated on the synthetic beat-wavelength. Figure 24(a) shows the investigated sample of a nominal step height of 1.34 μm . The single-shot dual-wavelength off-axis interferogram of the investigated sample is shown in Fig. 24(b). The filtering widows A and B as shown in Fig. 24(c) for $\lambda_1 = 635nm$ and $\lambda_2 = 675nm$, respectively, have been chosen carefully. The reconstructed amplitude and phase map for $\lambda_1 = 635nm$ and for $\lambda_2 = 675nm$ are shown in Fig. 24(d-e) and Fig. 24(e-f), respectively. The phase map on the synthetic beat-wavelength is shown in Fig. 24(h). The two dimensional (2D) surface profile along the selected line of Fig.24(h) is shown in Fig.24(i) after converting to height by using Eq.(23). The noise shown in Fig.24(i) is inevitable noise may come from the spatial filtering window and 2D-FFT processes. The noise vibration shown in Fig.24(i) is not coherent but varies sinusoidally; thus, it is more logical to express the height error as the root mean square (rms) value of the disturbed height (Malacara, et al., 2005). The rms height can be expressed as (Pan, et al., 2011):

$$h_{rms} = \sqrt{\left[h - \bar{h}\right]^2 / (N-1)}\,, \tag{24}$$

where h denotes the height distribution, $\bar{h}$ denotes the mean values, N represents the pixel number of row of calculation region. The modified height profile of Fig.24(i) after applying the rms for the distributed height is shown in Fig.25. The proposed rms method can provide a satisfied solution especially for measuring objects having high abrupt height difference. Based on the measured height in Fig.25, the average step height has been estimated to be around 1.30 μm .

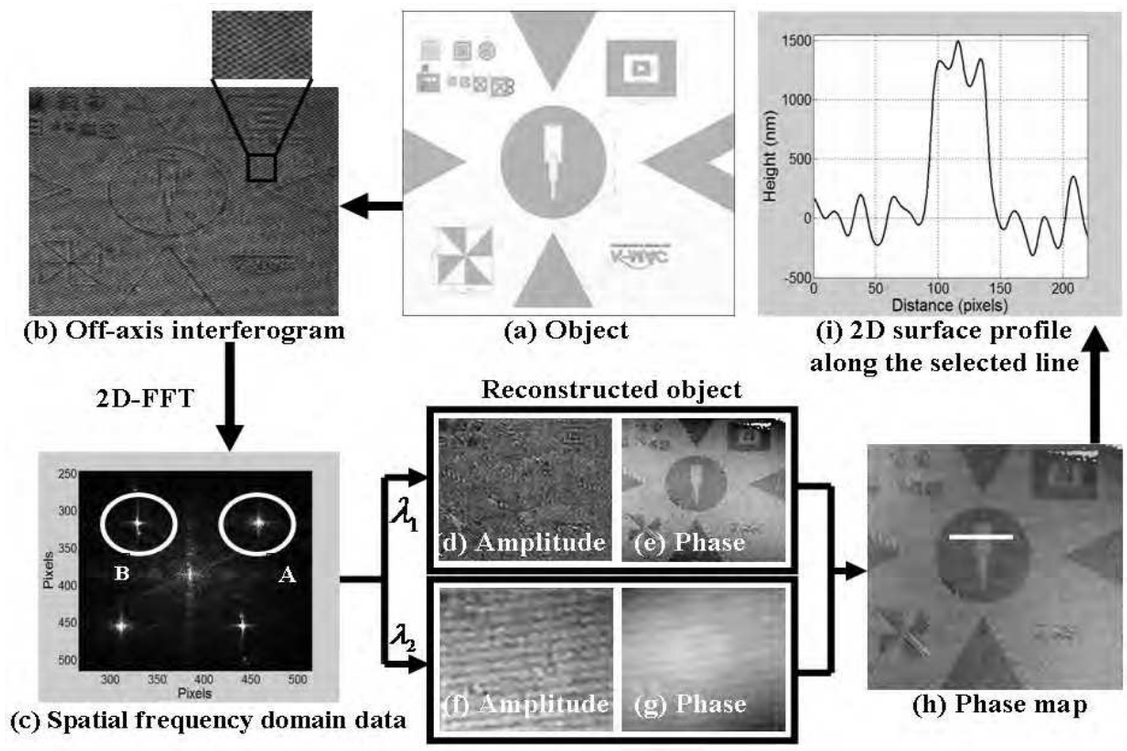

Fig. 24. Sequential reconstruction steps of the spatial filtering based phase contrast dual-wavelength off-axis interferometry (a) original phase object, (b) off-axis interferogram, (c) Fourier transformed spatial frequency domain data, (d)-(e) reconstructed amplitude and phase map for $\lambda_1 = 635nm$, (f)-(g) amplitude and phase map for $\lambda_2 = 675nm$, (h) object phase map on the synthethic beat-wavelength, and (i) two dimensional (2D) surface profile along the selected line of (h).

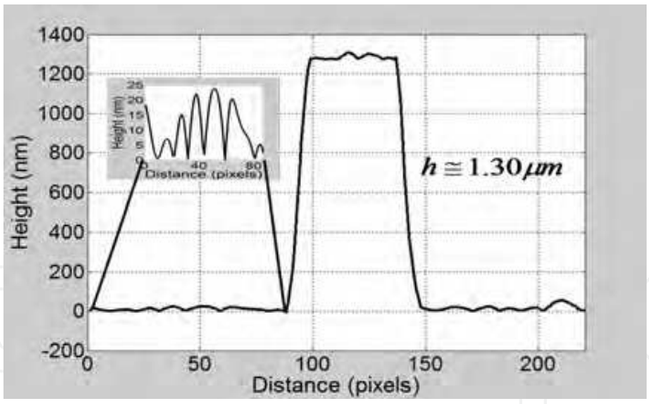

Fig. 25. Two-dimensional surface profile of Fig.24(i) after applying the rms method for the distributed height.

6. Multiple-beam interferometry

Multiple-beams interferometry means the generation of interference between reflected wavefronts from two surfaces, employing a succession of coherent beams. Such beams can combine and produce highly sharpened fringes. The earliest multiple-beam interferometers were developed by Fabry and Perot for the accurate measurement of wavelengths and the standard meter. Tolansky (Tolansky, 1960) studied the microtopography of different types of surfaces by using multiple-beam wedge interferometry (Fizeau-Tolansky type). However, the fact that the Fizeau-Tolansky wedge had an angle at the edge introduced many sources of difficulties which were the subject of many studies in the period (1945-1975). Sharp fringes are obtained when the surfaces forming the cavity are coated with higher reflectivity film (silver film is used here). The fringes obtained are called multiple-beam fringes. The theory of the intensity distribution of Fabry-Perot fringes at reflection from an infinite number of beams collected was dealt with by Holden (Holden, 1949). In the use of multiple beam interferometry several differences are encountered to the more conventional two-beam systems. In the two-beam case, the recorded intensity variation follows the Cos^2 law, which achieves an error estimation of (λ/2) for simple fringe counting. In contrast, multiple beam fringes are extremely sharp and simple measurements with such fringes can reveal surface micro topography close to (λ/500). The narrowness of the multiple-beam reflected fringes as shown in Fig.26 reflects directly on the accuracy with which the position of the fringe can be determined.

Figure.27 shows a schematic representation of the Fabry-Perot (F-P) interferometer in reflection. It shows that the air gap between the two plates is constant. The coating layer of the lower component is opaque while the upper component facing the incident light is semi transparent. The reflected rays are of the following amplitudes $r_1, r_3t^2, r_2r_3^2t^2, r_2^2r_3^3t^2, \ldots\ldots$. When the series is taken to infinity, the intensity distribution in the reflected system (Holden, 1949) is given as follows:

$$I_{R(\infty)} = r_1^2 + \frac{[t^4 r_3^2 + 2t^2 r_1 r_3 \cos(F+\delta) - 2t^2 r_1 r_2 r_3^2 \cos(F)]}{[1 + r_2^2 r_3^2 - 2r_2 r_3 \cos(\delta)]}. \quad (25)$$

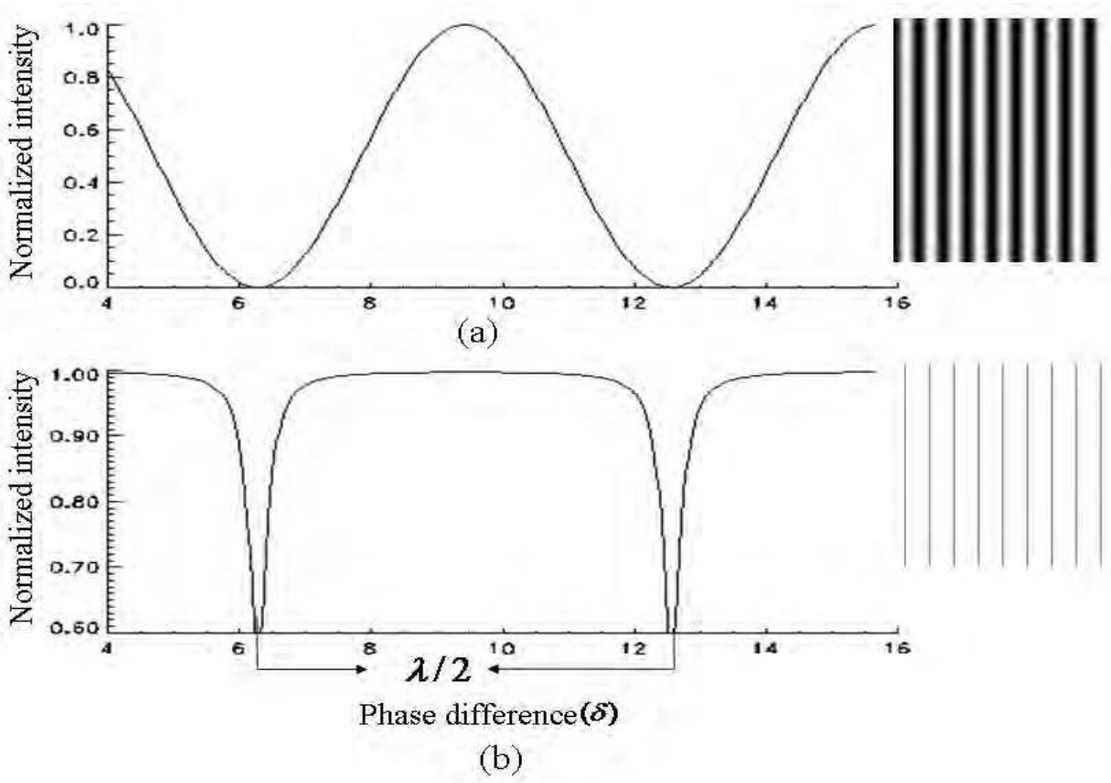

Fig. 26. (a) Two-beam cosine fringes. (b) Multiple beam Fabry-Perot fringes.

Where $r_1^2 = R_1$, $r_2^2 = R_2$ are the fractions of the light intensity reflected from the glass/metallic layer and air/metallic layer of the upper component, respectively. Also, $r_3^2 = R_3$ refers to the reflected intensity at air/metallic layer coating from the lower component, and $t^2 = T$ is the transmitted intensity through the metallic layer of the upper component. F is the combined phase function $F = 2\gamma - \beta_1 - \beta_2$. The phase difference δ between any two successive beams is given as follows:

$$\delta = \frac{2\pi}{\lambda}(2\mu t Cos(\theta)) \pm 2\beta \pm 2\gamma \,. \tag{26}$$

Where β_2 and β_3 are the change of phase at air/metallic layer reflection for the upper and lower components respectively and γ is the phase change in transmission. β_1 is the change of phase at glass/metallic layer reflection for the upper component of the interferometer when facing the incident light.

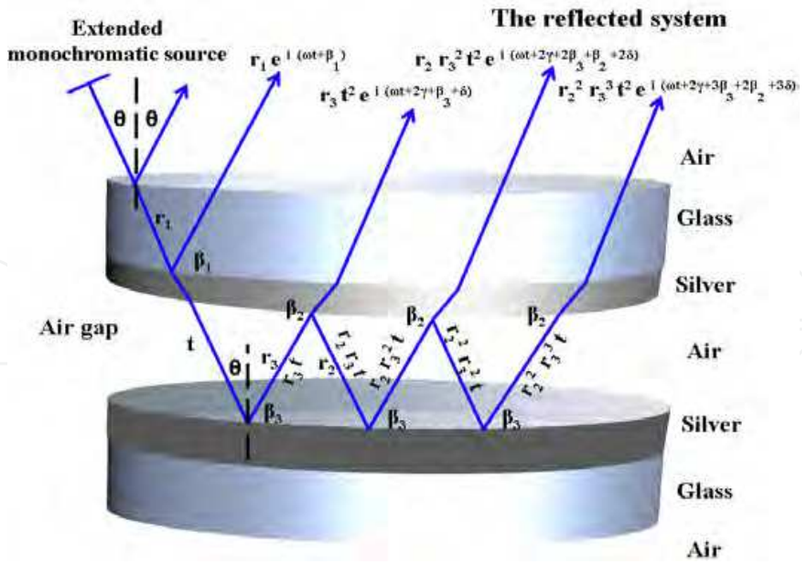

Fig. 27. Schematic representation of the Fabry-Perot (F-P) interferometer in reflection.

Figure.28(a) shows a schematic diagram of the Fizeau-Tolansky interferometer in reflection with coated inner surfaces producing fringes of equal thickness. Figure.28(b) shows a schematic diagram of the expected locations of the fringes in the Fizeau-Tolansky interferometer. Apparently, the fringe formation suffers from the existence of the wedge angle α causing a departure from the exact phase condition. Many authors discussed that effect (Gehrcke, 1906, Kinosita, 1953).The phase lag was estimated by Tolansky to be $\varepsilon = (4/3)\pi M^3 \alpha^2 N$ (Tolansky, 1960). Where M is the order of the last beam of effective amplitude contributing to the point of peak intensity, α is the wedge angle and N is the order of interference. In this section, a multiple-beam Fizeau-Tolansky interferometer in reflection for measuring the microtopography of an optical flat nominally of $\lambda/20$ is described (Abdelsalam et al., 2010). The method used for the fringe analysis is the Bünnagel's method (see section 4.3).

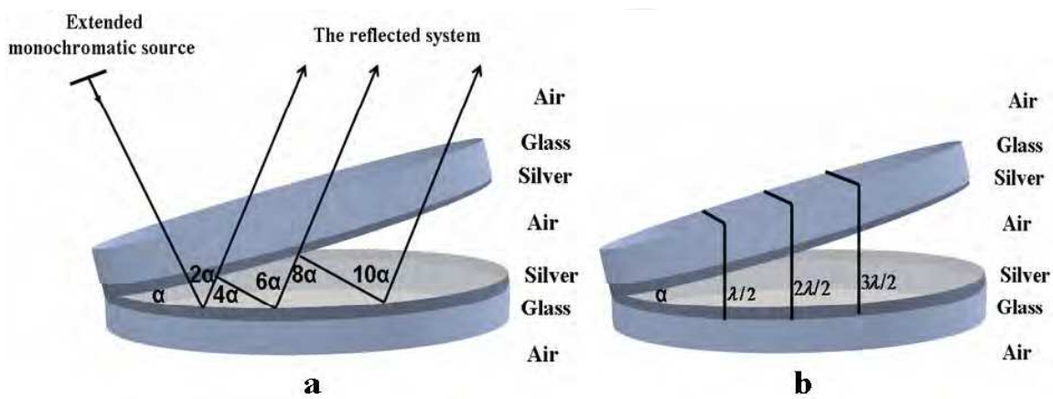

Fig. 28. The wedge interferometer (a) a schematic diagram of the Fizeau-Tolansky interferometer in reflection and (b) a schematic diagram of the expected locations of the fringes in the Fizeau-Tolansky interferometer.

The schematic diagram of the optical set up is illustrated in fig.29. The He-Ne laser source of 632.8 nm wavelength is allowed to pass through a beam expander of pinhole diaphragm diameter 20μm, where the beam diameter is expanded by a factor of 15. This is necessary for uniformly illuminating a greater area of the surface to be imaged and to reduce the error in measurement due to inhomogeneity in the Gaussian beam. The collimated beam of laser light falls upon the beam splitter which transmits one half and reflects one half of the incident light with constant phase change. The plates of the interferometer are coated with silver film of reflectivity nearly 90% which corresponding to 37 nm thickness and are mounted close together, with separation *t*. The reflected collimated beam is then incident on the interferometer which changes the path length of the light inside it due to the irregularities of the surface of the interferometer. When the reflected beams are combined, the intensity of the fringes is given by Eq.25. The interferogram was captured by the CCD camera and then refined by using flat fielding.

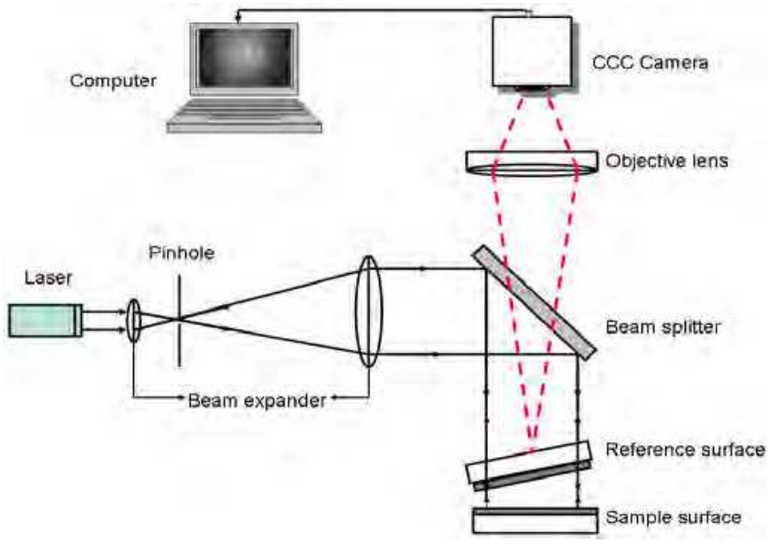

Fig. 29. Schematic diagram of the optical setup.

The average of 100 images captured by CCD camera is shown in Fig. 30(a). The corrected interferogram of Fig. 30(a) using flat fielding is shown in Fig. 30(b).

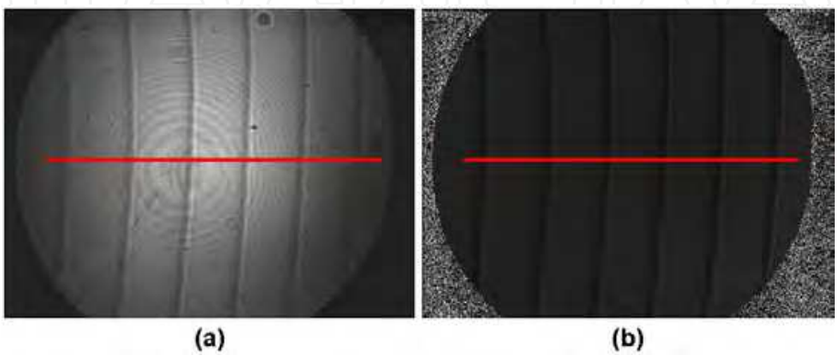

Fig. 30. (a) Average of one hundred images taken from the setup. (b) The corrected interferogram of (a).

Fig. 31(a) shows the profile taken at the middle of fig.30(a) as immersed in the background due to effect of the offset of the camera and the inhomogeneity of the collimated laser beam intensity. Fig.31(b) shows the profile taken at the middle of fig.30(b) after correction when the harmful background was removed i.e. was subtracted from the obtained distribution.

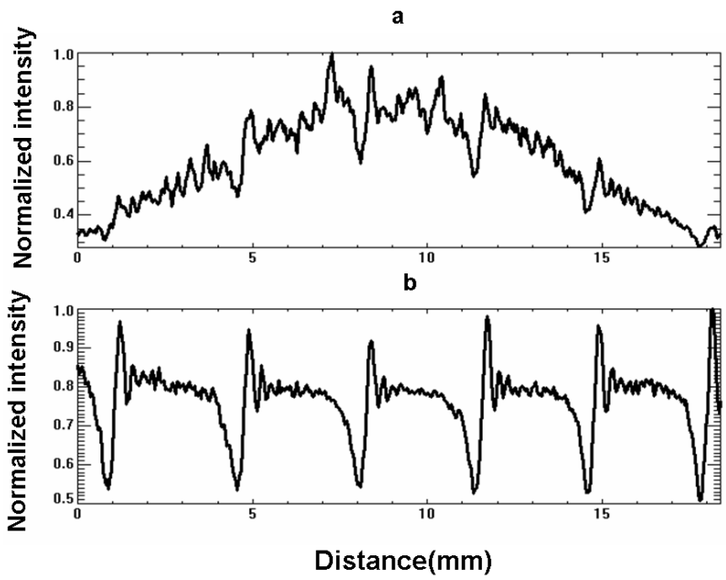

Fig. 31. Normalized intensity against distance along profile for average of one hundred images.(a) Before correction with flat fielding.(b) After correction with flat fielding.

The object surface with flatness $\lambda/20$ was tested using a calibrated reference of $\lambda/50$ flatness. Equation (11) has been applied into the corrected image (Fig.30 (b)) to get the topographical height as shown in fig.32. It was found that the peak to valley height of the optical flat equals $4.03x10^{-5}mm$ i.e. $\cong \lambda/16$. To obtain the form with high accuracy, ten profiles were calculated every 30 pixel in y axis and it was found that the mean of 10 values of the height for 10 different cross sections in the corrected interferogram was calculated as:

Total height (mm) = (4.03+3.62+3.88+4.25 + 3.08+3.49+3.54+3.98+4.15+4.59)x10^{-5}/10 = 3.86 x 10^{-5}(mm) $\cong \lambda/17$.

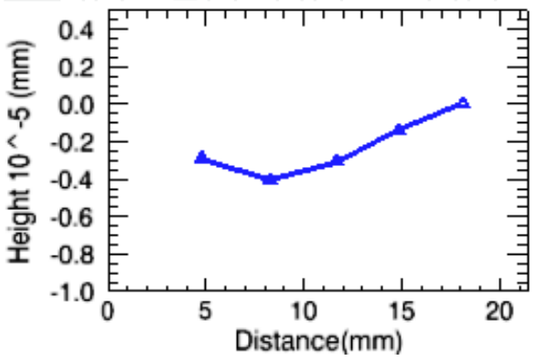

Fig. 32. Surface height (mm) measurement of a standard optical flat of nominally $\lambda/20$ resulted from one interferogram.

Because of there is no data between any two successive fringes in multiple beam case, phase shifting technique in multiple-beam is used to span the distances between the fringes. The scanning here is very important for obtaining good results and high measurement accuracy by increasing the number of points.

6.1 Phase shifting technique in multiple-beam interferometry

The basic idea of phase shifting technique is that, if the amplitude difference between the interfering beams is made to vary in some known manner such as changing in discrete steps (stepping), the intensities of the fringes are changed and hence the fringes are shifted. The most common way to vary the intensity distribution is to mount the object surface on a piezoelectric transducer (PZT) and change the voltage to the PZT. The calculations are based on an assumption that the PZT is linear in its motion. The distance of the cavity has been changed by varying the voltage and the displacement was measured precisely using laser interferometer. The voltage was applied and was varied four times as shown in the table 1. The distance inside the cavity is changed and then the fringe positions are changed. For each displacement one hundred images were captured using CCD camera and then corrected with flat fielding as show in Fig.33.

Voltage (V)	10	15	20	25
Distance (nm)	40	140	240	340

Table 1.Voltage versus distance.

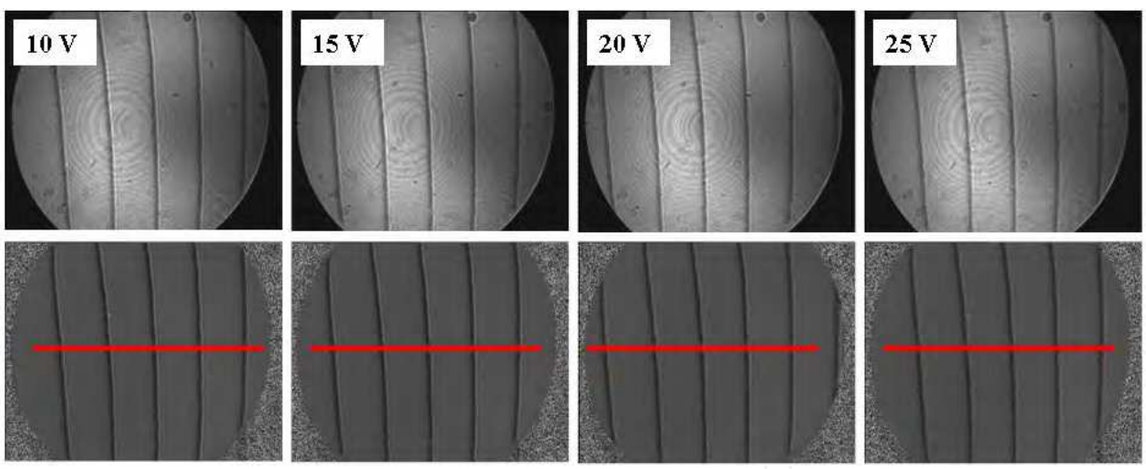

Fig. 33. Average of one hundred images and their corresponding corrections with flat fielding for 10V, 15V, 20V, and 25V.

The profiles of one cross section from the middle of the four interferograms have been illustrated in fig.34. The feature height of the optical flat was calculated for the four interferograms using Eq. (11). It was observed that there is a fluctuation in the regulations of the data which may be produced from the reading of the laser interferometer. This may be overcome using a programming process to get exactly the positions of the fringes. The data were arranged and sorted to obtain the feature height in one profile as shown in fig.35. The peak to valley value was calculated from fig.35 to be of the order of $\lambda/20$.

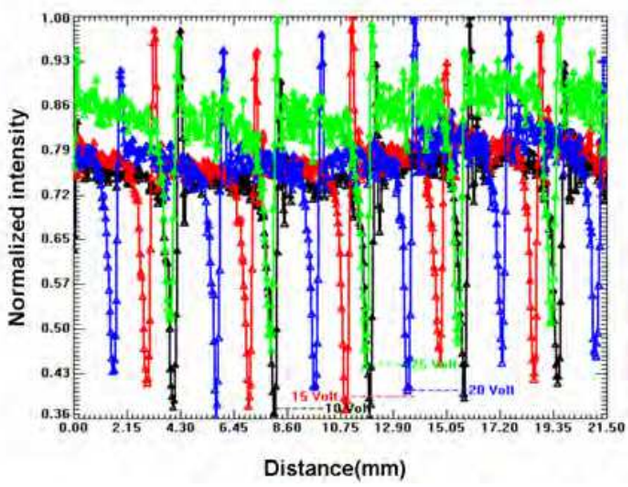

Fig. 34. The profiles of one cross section from the middle of the four interferograms for 10V,15V,20V, and 25V.

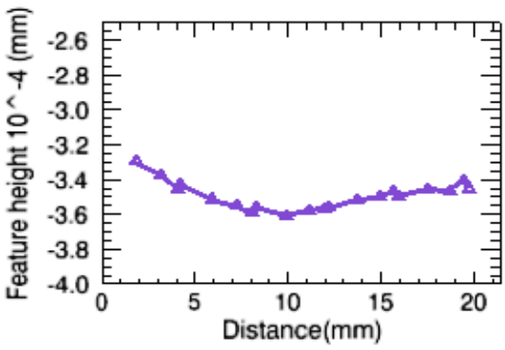

Fig. 35. Surface topography measurement of a standard optical flat of nominally λ / 20 resulted from the four interferograms.

7. Conclusion

In conclusion, we have presented the recent developments of interferometry techniques for surface micro topography measurement. In this chapter, a new approach to reduce coherent noise in interferometry phase-contrast image is presented. It is accomplished by combining the flat fielding method with the apodized apertures technique. In this chapter, different numerical reconstruction algorithms are reviewed and compared. Finally, we have described the principle of multiple-beam interferometry and its ability to feature very small height objects. Experimental results are presented to verify the principles.

8. Acknowledgment

Most of the work has been done in NIS (Egypt), Chonbuk National University (South Korea), and PTB (Germany). The Author would like to thank Dr. Daesuk Kim, Mechanical System Engineering Division, Chonbuk National University, South Korea and Dr. Michael Schulz, head of the Working Group "Form and Wavefront Metrology", PTB, Germany for data analysis.

9. References

Abdelsalam, D. ; Magnusson, R.; & Kim, D. (2011). Single-shot dual wavelength digital holography based on polarizing separation, Applied Optics, 50, pp. 3360-3368.

Abdelsalam, D.; & Kim, D. (2011). Coherent noise suppression in digital holography based on flat fielding with apodized apertures, Optics Express, 19, pp. 17951-17959.

Abdelsalam, D.; Baek, B.; Cho, Y.; & Kim, D. (2010). Surface form measurement using single-shot off-axis Fizeau interferometer, J. Opt. Soc. Korea, 14, pp. 409-414.

Abdelsalam, D.; Shaalan, M.; & Eloker, M. (2010). Surface microtopography measurement of a standard flat surface by multiple-beam interference fringes at reflection, Optics and Lasers in Engineering, Vol. 48, pp. 543-547.

Abdelsalam, D.; Shaalan, M.; Eloker, M.; & Kim, D. (2010). Radius of curvature measurement of spherical smooth surfaces by multiple-beam interferometry in reflection, Optics and Lasers in Engineering, Vol. 48, pp. 643-649.

Born, M.; Wolf, E. (1980). Principles of Optics, Cambridge University Press, pp 459-490.

Bünnagel, R. (1956). Einfaches verfahren zur topographischen darstellung einer optischen planflache. Opt Acta, 3, pp. 81-85.

Cuche, E. ; Marquet, P.; & Depeursinge, D. (2000). Spatial filtering for zero-order and twin image elimination in digital off-axis holography, Applied Optics, 39, pp. 4070-4075.

Cuche, E.; Bevilacque, F.; & Depeursinge, C. (1999). Digital holography for quantitative phase contrast imaging, Optics. Letters., 24, pp. 291-293.

Cuche, E.; Marquet, P.; & Depeursinge, C. (2000). Aperture apodization using cubic spline interpolation :application in digital holographic microscopy, Optics communications, 182, pp. 59-69.

David, F.; John, T.; Lopez, R.; & Stahl, H. (1993). Vector formulation for interferogram surface fitting, Applied Optics, 32, pp. 4738-43.

Gabor, D. (1948). A new microscopic principle, Nature, 161, pp. 777-778.

Gehrcke, E. (1906). Interferenzen, pp 39, Germany.

Ghiglia, D. ; & Pritt, M. (1998). Two-dimensional Phase Unwrapping : Theory, Algororithm, and Software, Wiley, New York , USA.

Holden, J. (1949). Multiple-beam interferometer-intensity distribution in the reflected system, Proc. Phys. Soc., 62, pp. 405-417.

Kinosita, K. (1953). Numerical evaluation of the intensity curve of a multiple-beam Fizeau fringe, J. Phys. Soc. Japan, 8, pp. 219-225.

Kühn, J.; Colomb, T.; Montfort, F.; Emery, Y.; Cuche, E.; & Depeursinge, C. (2007). Real-time dual-wavelength digital holographic microscopy with a single hologram acquisition, Optics Express, 15, pp. 7231-42.

Kumar, U. ; Bhaduri, B. ; Kothiyal, M. ; & Mohan Krishna. (2009). Two wavelength micro-interferometry for 3-D surface profiling, Optics and Lasers in Engineering, 47, pp. 223-229.

Malacara, D. ; Servin, M.; & Malacara, Z. (2005). Interferogram analysis for optical testing, United States of America : Taylor and Francis Group, pp. 384-385.

Pan, F.; Xiao, W.; Liu, S. ; Wang, F., & Li, R. (2011). Coherent noise reduction in digital holographic phase contrast microscopy by slightly shifting object, Optics Express, 19, pp. 3863-3869.

Steve, B. (2006). Hand book of CCD astronomy, Cambridge, UK.

Tolansky, S. (1960). Surface microtopography, London : Longmans.

Wang, JY.; & Silva, DE. (1980). Wave-front interpretation with Zernike polynomials. Applied Optics, 19, pp. 1510-8.

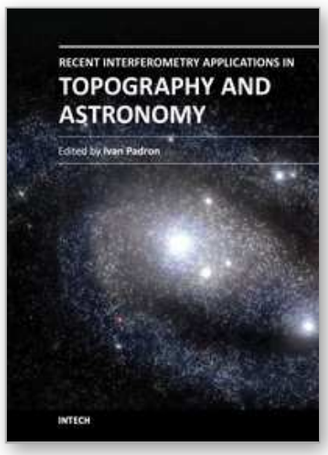

Recent Interferometry Applications in Topography and Astronomy
Edited by Dr Ivan Padron

ISBN 978-953-51-0404-9
Hard cover, 220 pages
Publisher InTech
Published online 21, March, 2012
Published in print edition March, 2012

This book provides a current overview of the theoretical and experimental aspects of some interferometry techniques applied to Topography and Astronomy. The first two chapters comprise interferometry techniques used for precise measurement of surface topography in engineering applications; while chapters three through eight are dedicated to interferometry applications related to Earth's topography. The last chapter is an application of interferometry in Astronomy, directed specifically to detection of planets outside our solar system. Each chapter offers an opportunity to expand the knowledge about interferometry techniques and encourage researchers in development of new interferometry applications.

INTECH
open science | open minds

InTech Europe
University Campus STeP Ri
Slavka Krautzeka 83/A
51000 Rijeka, Croatia
Phone: +385 (51) 770 447
Fax: +385 (51) 686 166
www.intechopen.com

InTech China
Unit 405, Office Block, Hotel Equatorial Shanghai
No.65, Yan An Road (West), Shanghai, 200040, China
中国上海市延安西路65号上海国际贵都大饭店办公楼405单元
Phone: +86-21-62489820
Fax: +86-21-62489821

IntechOpen